Soft Matter

PAPER

View Article Online
View Journal

Cite this: DOI: 10.1039/c4sm00066h

The molecular structure of a phosphatidylserine bilayer determined by scattering and molecular dynamics simulations†

Jianjun Pan,*[a] Xiaolin Cheng,[bc] Luca Monticelli,[de] Frederick A. Heberle,[b] Norbert Kučerka,[fg] D. Peter Tieleman[h] and John Katsaras*[bij]

Received 10th January 2014
Accepted 6th February 2014

DOI: 10.1039/c4sm00066h

www.rsc.org/softmatter

Phosphatidylserine (PS) lipids play essential roles in biological processes, including enzyme activation and apoptosis. We report on the molecular structure and atomic scale interactions of a fluid bilayer composed of 1-palmitoyl-2-oleoyl-*sn*-glycero-3-phosphatidylserine (POPS). A scattering density profile model, aided by molecular dynamics (MD) simulations, was developed to jointly refine different contrast small-angle neutron and X-ray scattering data, which yielded a lipid area of 62.7 Å^2 at 25 °C. MD simulations with POPS lipid area constrained at different values were also performed using all-atom and aliphatic united-atom models. The optimal simulated bilayer was obtained using a model-free comparison approach. Examination of the simulated bilayer, which agrees best with the experimental scattering data, reveals a preferential interaction between Na^+ ions and the terminal serine and phosphate moieties. Long-range inter-lipid interactions were identified, primarily between the positively charged ammonium, and the negatively charged carboxylic and phosphate oxygens. The area compressibility modulus K_A of the POPS bilayer was derived by quantifying lipid area as a function of surface tension from area-constrained MD simulations. It was found that POPS bilayers possess a much larger K_A than that of neutral phosphatidylcholine lipid bilayers. We propose that the unique molecular features of POPS bilayers may play an important role in certain physiological functions.

1. Introduction

In mammalian cell membranes the aminophospholipid phosphatidylserine (PS) comprises 2–10% of total phospholipid[1] and plays a pivotal role in a number of biological processes. Specifically, PS has been found to regulate membrane surface charge, and serves as a stereospecific binding partner for globular domains.[2] PS also acts as an important cofactor for virus infection,[3] promotes vesicle endocytosis,[4] signals the initiation of the coagulation cascade,[5] and is required for optimal protein targeting and activation during cell division.[6] Importantly, the externalization of PS from the inside to the outside of a cell – likely facilitated by scramblase activation coupled with flippase inactivation – initiates the pathway of programmed cell death.[7,8]

Despite its physiological importance, structural studies of PS membranes have been few, and molecular dynamics (MD) simulations of charged PS bilayers have been hampered by the lack of experimental structural data. Previous MD simulations of a 1-palmitoyl-2-oleoyl-*sn*-glycero-3-phosphatidylserine (POPS) bilayer produced an area per lipid of 55 Å^2 at 27 °C,[9] a value about 10 Å^2 smaller than its zwitterionic counterpart, 1-palmitoyl-2-oleoyl-*sn*-glycero-3-phosphatidylcholine (POPC). Although some PS lipid structural information should be transferable from accurately determined PC structures, differences in headgroup electrostatics, including interactions with ions, can alter the balance of forces that give rise to bilayer structure.[10] Indeed, small perturbations of these forces can result in relatively large changes to some structural parameters, including the area per lipid. For this reason, simulated structures must be carefully validated with experimental data.

[a]Department of Physics, University of South Florida, Tampa, FL 33620, USA. E-mail: panj@usf.edu

[b]Oak Ridge National Laboratory, Oak Ridge, TN, 37831 USA. E-mail: katsarasj@ornl.gov

[c]Department of Biochemistry and Cellular and Molecular Biology, University of Tennessee, Knoxville, TN 37996, USA

[d]INSERM, UMR-S665, Paris, F-75015, France

[e]INTS, Paris, France

[f]Canadian Neutron Beam Centre, National Research Council, Chalk River, Ontario, Canada K0J 1J0

[g]Department of Physical Chemistry of Drugs, Faculty of Pharmacy, Comenius University, 832 32 Bratislava, Slovakia

[h]Department of Biological Sciences and Centre for Molecular Simulation, University of Calgary, 2500 University Drive NW, Calgary, AB, Canada T2N 1N4

[i]Department of Physics and Astronomy, University of Tennessee, Knoxville, TN 37996, USA

[j]Joint Institute for Neutron Sciences, Oak Ridge National Laboratory, Oak Ridge, TN, 37831, USA

† Electronic supplementary information (ESI) available. See DOI: 10.1039/c4sm00066h

In this study we used different contrast small-angle neutron (SANS) and X-ray (SAXS) scattering data, in conjunction with MD simulations utilizing two different force fields, to determine the structure of a fluid POPS bilayer. Specifically, we developed a scattering density profile (SDP) model to jointly refine SANS and SAXS data. Bilayer structural parameters such as bilayer thickness and area per lipid were determined from this model-based approach. We also performed multiple sets of area-constrained MD simulations. A model-free comparison of these simulations to the experimental scattering data revealed the "best" simulated bilayer, from which additional structural features and mechanical properties of the POPS bilayer were determined.

2. Materials and methods

2.1 Small-angle neutron and X-ray scattering

Synthetic POPS (sodium salt) was purchased from Avanti Polar Lipids (Alabaster, AL) and was used as received. The molecular volume of POPS was determined using a vibrating tube density meter, as described in ESI Section S1.† Unilamellar vesicles (ULVs) for scattering experiments were prepared as previously described.[11,12] Briefly, 40 mg of POPS was mixed with 1.0 ml of D_2O buffer, followed by freeze–thaw cycling between −80 and 45 °C. The lipid dispersion was extruded using an Avanti mini-extruder outfitted with a 50 nm diameter pore size polycarbonate filter. The resulting ULV suspension was divided into three microcentrifuge tubes and diluted to the desired external contrast condition (*i.e.*, 100, 75 and 50% D_2O) using an appropriate ratio of D_2O and H_2O buffers. The final lipid concentration was about 12 mg ml^{-1}. ULVs for SAXS measurements were prepared in a similar manner using H_2O buffer.

Three buffer conditions were used for this study, namely: (1) pure water; (2) 5 mM 4-(2-hydroxyethyl)piperazine-1-ethanesulfonic acid (HEPES) at pH 7.4; and (3) 5 mM HEPES/100 mM NaCl at pH 7.4. No measurable differences in POPS bilayer structure were observed for the different conditions (ESI Section S2†). Therefore, for purposes of clarity we present only the scattering data for POPS ULVs suspended in pure water. The obtained SANS and SAXS intensity I (ESI Sections S3 and S4†) as a function of scattering vector Q was converted into neutron (nFF) and X-ray (xFF) form factors using the relationship $\mathrm{FF} = Q \times \mathrm{sign}(I) \times \sqrt{|\mathrm{I}|}$, where FF corresponds to nFF or xFF, and sign(I) refers to the sign of the intensity I (*i.e.*, plus or minus for positive and negative intensities, respectively).

2.2 Molecular dynamics simulations

2.2.1 Simulations using CHARMM package. The CHARMM-GUI Membrane Builder[13] was used to generate coordinates for a POPS bilayer containing 128 lipids total. Hydrogen atoms were explicitly included for the entire lipid molecule (all-atom model), including 5385 water molecules and a sufficient amount of NaCl to prepare a salt concentration of 100 mM. MD simulations were performed using the NAMD 2.8 (ref. 14) and CHARMM 36 lipid force field.[15,16] Periodic boundary conditions were enforced. For each system, atomic coordinates were first minimized using the conjugated gradient algorithm for 5000 steps, followed by 2 ns of equilibration for a constant particle number, pressure, and temperature (*NPT*) ensemble. Equilibrium was determined by monitoring the system's area per lipid and the root-mean-square deviation (RMSD). In all simulations, the van der Waals (vdW) interactions were truncated *via* a potential-based switching function used by X-PLOR. Starting from a switching distance of 10.5 Å, the vdW potential was brought smoothly to 0 at the cutoff distance of 12 Å. Electrostatic interactions were treated using the particle-mesh Ewald (PME) method with a 1.0 Å grid spacing.[17,18] The r-RESPA multiple-time-step method[19] was employed with a 2 fs time step for bonded, and 2 and 4 fs time steps for short-range non-bonded and long-range electrostatic interactions, respectively. The bonds between hydrogen and other atoms were constrained using the SHAKE algorithm.[20]

We first simulated the POPS bilayer using the *NPT* ensemble for 40 ns. Langevin dynamics were used to maintain a constant temperature of 298 K, while the Nosé-Hoover Langevin-piston algorithm[21,22] was used to maintain a constant pressure of 1 bar. The z-axis was allowed to expand and contract independently of the x–y plane (semi-isotropic pressure coupling). The result from this simulation was used to guide the development of an SDP model for the subsequent analysis of neutron and X-ray scattering data.

An additional twelve sets of constant particle number, area, normal pressure, and temperature (NAP_nT) simulations were performed, where the average lipid areas were constrained to 54.5, 56.0, 57.5, 59.0, 60.5, 62.0, 63.0, 64.0, 65.1, 66.2, 67.2 and 68.2 $Å^2$, while the z-axis was allowed to expand and contract in order to maintain a constant P_n. The starting configurations for these simulations were selected snapshots from the *NPT* trajectory with a lipid area close to the target value. The production run length for each of these simulations was between 79 and 114 ns. Only the final 50 ns from each trajectory were used for data analysis. All simulations were conducted on the Hopper supercomputer located at the National Energy Research Scientific Computing Center (NERSC).

The lipid bilayer area compressibility modulus K_A is defined as:[23]

$$K_A = [\partial\gamma/\partial(\ln A)]_T, \quad (1)$$

where γ is the surface tension and A is the lipid area. For each simulated area A the surface tension γ was calculated from the difference between the normal [$p_N = p_{zz}$] and lateral [$p_L = (p_{xx} + p_{yy})/2$] components of the pressure tensor in the simulation as follows:

$$\gamma = \int[P_N(z) - P_L(z)]\mathrm{d}z. \quad (2)$$

The lateral pressure profile as a function of the z-coordinate was calculated with NAMD, based on the algorithm of Lindahl and Edholm[24] and Sonne *et al.*[25]

2.2.2 Simulations using GROMACS package. Initial POPS bilayer coordinates and force field were taken from Mukhopadhyay *et al.*[9] The force field is consistent with the Berger parameter set,[26] which uses a united atom representation for

the hydrocarbon chains and explicit hydrogens for polar moieties (aliphatic-united-atom model). Lennard–Jones interactions for the acyl chains were taken from Berger *et al.*;[26] for all other atom types, Lennard–Jones parameters were from OPLS.[27,28] Partial charges on the lipid backbone were assigned similar to the work of Chiu *et al.*,[29] and bonded interactions were based on the GROMOS87 force field[30] (implemented in GROMACS as ffgmx). Partial charges for the carboxylate group were taken from the aspartic acid side chain in ffgmx. We will refer to this force field as GROMACS, in contrast to the CHARMM force field which is described in Section 2.2.1.

The system contained a total of 128 lipids, 5391 SPC water molecules, and 150 mM NaCl. All simulations were carried out using the GROMACS 4.5 software package.[31] Two types of simulations were performed, depending on the treatment of the average lipid area, namely: (1) for *NPT* simulations a semi-isotropic pressure coupling of 1 bar was applied, thus allowing the area per lipid to vary; and (2) in NAP_nT simulations, the average lipid area was fixed in the x–y plane and 1 bar of pressure was applied in the z direction. The lipid area determined from unconstrained simulations was 52.0 Å^2, while average areas of 65.1 and 67.5 Å^2 were chosen for constrained simulations. In both cases, pressure was maintained using the Parrinello–Rahman barostat[32] with a time constant of 4 ps and compressibility of 4.5×10^{-5} per bar. Lipid and solvent (including ions) were coupled separately to a temperature bath at 298 K using the Bussi–Donadio–Parrinello thermostat (v-rescale)[33] with a coupling constant of 1 ps.

A leapfrog integrator was used with a 2 fs time step. All bonds were constrained to their equilibrium values using the SETTLE algorithm[34] for water, and the LINCS algorithm[31,35] for all other bonds. A cutoff of 1.0 nm was used for calculating the Lennard–Jones interactions. Electrostatic interactions were evaluated using the PME method.[17,18] Real space interactions were evaluated using a 1.0 nm cutoff, and reciprocal–space interactions were evaluated on a 0.12 nm grid using a fourth-order spline interpolation. Simulation times were 100 ns and 300 ns for unconstrained- and constrained-area simulations, respectively, with atomic coordinates recorded every picosecond. Only the final 40 ns of each simulation trajectory were used, and were analyzed using GROMACS.

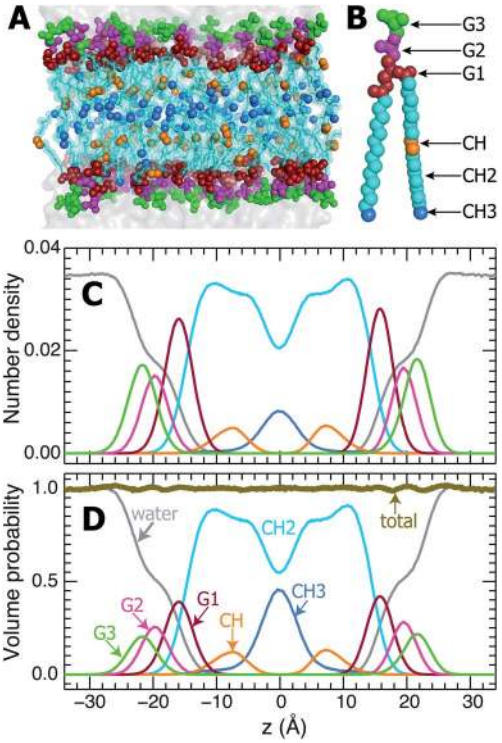

Fig. 1 POPS bilayer component distributions. (A) A representative snapshot of the POPS bilayer. Components are colored following the scheme in (B) of an individual POPS molecule. The headgroup and hydrocarbon chains are each parsed into three components (*i.e.*, glycerol-carbonyl backbone G1, phosphate G2 and terminal serine G3 for the headgroup, and methine CH, methylene CH2 and terminal methyl CH3 for the hydrocarbon chains). Number density (C) and volume probability (D) distributions of each component were calculated after averaging a trajectory of NAP_nT simulations. The small deviations from unity (along z) of the total volume probability (thick gold line in D) are consistent with the assumption that there is no persistent vacancy along the bilayer normal.

3. Results

3.1 SDP model analysis of scattering data

Three sets of different contrast SANS data (*i.e.*, 100, 75 and 50% D_2O) and one set of SAXS data (100% H_2O) were obtained from POPS ULVs at 25 °C. Guided by preliminary MD simulations, an SDP model (Fig. 1) was developed to jointly refine the experimental datasets. The POPS headgroup and hydrocarbon chains were each parsed into three components, such that the individual component volume probability distributions were fully described by Gaussian and error functions (ESI Section S5†). We note that the approximation of the hydrocarbon chain region by two error functions precludes the possibility of water molecules residing in the bilayer center. This treatment is based on two considerations: (1) both SANS and SAXS measurements were performed on time scales much larger than the transient nature of water molecules in the hydrocarbon chain region;[36] and (2) the water concentration in the bilayer center is below the detection limit of one water molecule per lipid, as determined by magic angle spinning nuclear Overhauser enhancement spectroscopy.[37]

Fig. 2 shows the result from SDP analysis, which shows good agreement between experimental and model form factors (Fig. 2A and B), with the corresponding model neutron scattering length density (NSLD) and electron density (ED) profiles shown in Fig. 2C and D, respectively. When calculating the bilayer NSLD, it is particularly important to account for exchangeable hydrogens (ESI Section S6††). For example, within the PS headgroup, the terminal serine's ammonium ion possesses three rapidly exchangeable hydrogens. This is in contrast to phosphatidylcholine (PC) lipids, which do not contain exchangeable hydrogens. The PS bilayer's NSLD is therefore dependent on solvent D_2O concentration. For a solvent with a D_2O mole fraction c ($0 \leq c \leq 1$), a statistically representative ammonium possesses $3 \times c$ deuteriums and $3 \times (1 - c)$ hydrogens. We found that neglecting exchangeable hydrogens in the analysis artificially increases POPS' lipid area.

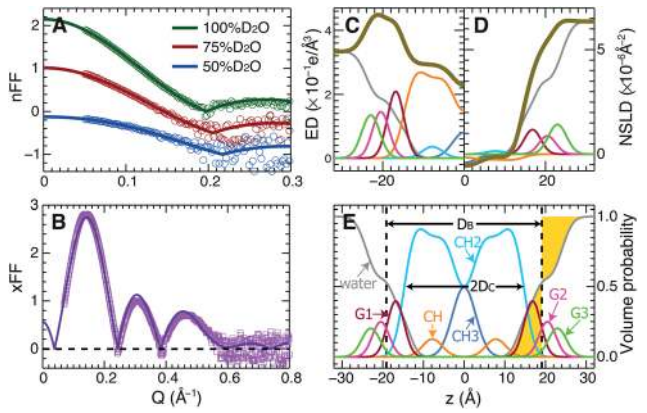

Fig. 2 SDP model analysis of experimental scattering data for a POPS bilayer. (A) Neutron form factors at three D_2O concentrations. (B) X-ray form factor. Electron density (C) and neutron scattering length density (D) distributions of bilayer components were calculated from the volume probability distributions (E), which were determined by jointly refining experimental neutron and X-ray form factors. The thick gold lines in (C) and (D) represent total electron density and neutron scattering length density (in 100% D_2O) profiles, respectively. Note that only one bilayer leaflet is shown in the electron density and neutron scattering length density distributions. The color scheme of each component is the same as in Fig. 1. The vertical dashed line separating two yellow-filled areas in (E) highlights the Gibbs dividing surface, which is located at the water/bilayer interface ($D_B/2$). The hydrocarbon chain thickness ($2D_C$) is defined by the total width of the two error functions representing the sum of the CH, CH2 and CH3 components.

Table 1 POPS bilayer structural parameters obtained from NAP_nT simulations (*i.e.*, CHARMM force field) and SDP model analysis. Double asterisks (**) in the last column denote fixed parameters during SDP model analysis, while a single asterisk (*) denotes "soft" constrained parameters with their target values in parentheses. The estimated uncertainties for lipid area and bilayer thicknesses are 2%.

	CHARMM	SDP model
A (Å^2)	62.0	62.7
V_L (Å^3)	1196.7	1198.5**
V_{HL} (Å^3)	289.2	278.0**
V_{CH2} (Å^3)	26.7	27.2
D_B (Å)	38.6	38.2
$2D_C$ (Å)	29.2	29.4
D_{HH} (Å)	40.6	42.2
D_{H1} (Å)	5.7	6.4
σ_{CH3} (Å)	3.0	2.9
r_{CH3}	2.1	2.0*(2.1)
z_{CH} (Å)	7.8	7.8*(7.8)
σ_{CH} (Å)	2.5	2.5*(2.5)
r_{CH}	0.9	0.9*(0.9)
z_{HC} (Å)	14.6	14.7
σ_{HC} (Å)	2.1	2.1*(2.1)
z_{G1} (Å)	15.9	16.8
σ_{G1} (Å)	2.1	2.0
r_{G1}	0.46	0.46*(0.46)
z_{G2} (Å)	19.6	20.5
σ_{G2} (Å)	2.0	2.1
r_{G2}	0.29	0.29*(0.29)
z_{G3} (Å)	21.6	22.9
σ_{G3} (Å)	2.2	2.2*(2.2)

A key feature of SDP analysis is the common description of ED and NSLD profiles, which are linked by the underlying component volume probability distributions (Fig. 2E). The component ED and NSLD profiles retain the same functional forms as the component volume probability distributions, and differ only by a scaling factor (the component's total number of electrons or neutron scattering length). SDP analysis therefore consists of finding component volumes (parameter set 1) and variables (parameter set 2) describing the volume probability distributions (*i.e.*, the width and position of Gaussian and error functions). Lipid bilayer structure is effectively defined by these two sets of parameters.[38] For example, the bilayer hydrocarbon chain thickness $2D_C$ is defined as the full width of the two error functions, which represent the total volume probability of the hydrocarbon chains (Fig. 2E). The overall bilayer thickness D_B is defined by the location where the integral of the water volume probability on the bilayer side equals the integral of water deficit on the solvent side (denoted by the yellow-filled areas on either side of the vertical dashed line in Fig. 2E). The area per lipid A is related to D_B through volumetric data, *i.e.*, $A = 2V_L/D_B$, where V_L is the lipid volume. A can also be calculated based on the hydrocarbon chain thickness D_C, *i.e.*, $A = V_{HC}/D_C$, where V_{HC} is the hydrocarbon chain volume.

The fitting parameters obtained from SDP model analysis of the POPS bilayer are listed in Table 1, in addition to a set of area-constrained MD simulations ($A = 62.0$ Å^2) using the CHARMM force field. Parameters include: (1) A, the area per lipid; (2) V_L, V_{HL}, and V_{CH2}, the volumes of the total lipid, lipid headgroup, and average methylene group in the hydrocarbon chain region, respectively; (3) D_B, $2D_C$, D_{HH}, and D_{H1} are, respectively, the overall bilayer thickness, bilayer hydrocarbon chain thickness, the headgroup–headgroup separation as determined by the distance between ED maxima, and the difference between $D_{HH}/2$ and D_C; (4) z_{HC} and σ_{HC} are the half-separation (same as D_C) and width of the two error functions, respectively, representing the total hydrocarbon chain region; (5) z_{CH}, σ_{CH}, and r_{CH} are, respectively, the Gaussian center, width, and the volume ratio V_{CH}/V_{CH2}, where V_{CH} and V_{CH2} refer to the average volume of the CH and CH2 components, respectively (the same notation was applied to the CH3 component to define σ_{CH3} and r_{CH3}); and (6) z_{G1}, σ_{G1}, and r_{G1} are, respectively, the Gaussian center, width, and volume fraction with respect to the total headgroup of the G1 component, with the same notation applied to the G2 and G3 components (*i.e.*, z_{G2}, σ_{G2}, r_{G2}, and z_{G3}, σ_{G3}).

To enhance the robustness of the nonlinear least-squares fitting algorithm, parameter space was restricted through a judicious choice of constraints which were guided by a combination of experimental and simulation data. Specifically, the total lipid volume was fixed to an experimentally determined value (ESI Section S1†). It is worth noting that the total lipid volume resulting from MD simulations is in good agreement with the experimental value (Table 1). Lipid headgroup volume V_{HL} is, however, more variable. In the present study we assumed that the total hydrocarbon chain volume of POPS is identical to POPC.[11] This assumption yields a POPS headgroup volume of 278.0 Å^3. To estimate structural uncertainties resulting from the headgroup volume uncertainty we performed SDP model

analysis by setting the headgroup volume to 250.2 or 305.8 Å^3 (*i.e.*, allowing for V_{HL} to deviate by as much as 10% from 278.0 Å^3). The resulting lipid area varies by less than 0.4%, which is well below the upper bound limit of 2% uncertainty that we estimate for lipid area and bilayer thicknesses based on current model analysis.[38,39]

In addition to the fixed total lipid and headgroup volumes, several soft constraints were applied, whereby deviation from a target value (taken from MD simulations) resulted in a quadratic penalty to the overall χ^2. Soft-constrained parameters include the ratios of the headgroup and acyl chain component volumes (r_{G1}, r_{G2}, r_{CH} and r_{CH3}), the width and center of the CH component (σ_{CH} and z_{CH}), the width of the hydrocarbon error function (σ_{HC}), and the width of the G3 component (σ_{G3}).

Finally, to avoid local minima, the fitting procedure was implemented as follows:

1. Let $t_{0,i}$ represent the initial guess for the ith fitting parameter whose deviation is assumed to be no greater than Δt_i. A random number $R_i \in [-1, 1]$ was generated with the initial value of the ith parameter taken as $t_i = t_{0,i} + \Delta t_i \times R_i$.

2. Step 1 was repeated for all fitting parameters to generate a set of input parameters $\boldsymbol{t}$.

3. The SDP analysis was performed using $\boldsymbol{t}$ to generate a set of best-fit bilayer structural parameters $\boldsymbol{t}_{SDP}$.

4. Steps 1–3 were repeated to generate an ensemble of $\boldsymbol{t}_{SDP}$, which in general depended on the initial input parameter set $\boldsymbol{t}$. If a subset of $\boldsymbol{t}_{SDP}$ (more than one set) exhibits the same structural parameters with the smallest χ^2, the best estimate of the SDP parameters were considered determined, otherwise the analysis produced no solution – most likely, each $\boldsymbol{t}_{SDP}$ set corresponds to local minima.

3.2 Model-free validation of simulated bilayers

It is not surprising that inaccuracies in MD force fields can result in bilayers with unphysical features. It is therefore essential to compare simulated bilayers to experimental data. In this work, a model-free validation of simulated bilayers was achieved by comparing experimental and simulated form factors, rather than derived structural parameters such as lipid area, which are affected by prior assumptions made during model analysis. Simulated bilayer form factors were obtained directly from MD trajectories by computing the number density distributions of all atoms, from which the NSLD and ED profiles were then obtained by summing the products of the number density of each atom by its corresponding neutron scattering length or electron number. Fourier transform of the solvent-subtracted NSLD or ED profile then gives rise to the simulation neutron or X-ray form factor. The quality of each simulation form factor was quantified by the reduced χ^2, which is defined as:

$$\chi^2 = \sqrt{\frac{1}{N-1}\sum_{i=1}^{N}\left(\frac{F_{\mathrm{sim},i} - k \times F_{\mathrm{exp},i}}{k \times \sigma_{F_{\mathrm{exp}}}}\right)^2}, \qquad (3)$$

where N is the number of experimental data points, i is the index referring to each data point, F_{sim} and F_{exp} are the simulation and experimental form factors, respectively, $\sigma_{F_{exp}}$ is the uncertainty of the experimental form factor, and k is a scaling factor that minimizes χ^2. When multiple experimental form factors are available, as was the case in the present study (*i.e.*, three different contrast SANS form factors and one SAXS form factor), the overall χ^2 is the sum of the individual χ^2 for each set of form factors. The most physically probable lipid bilayer produced by simulations is the one that generates the smallest overall χ^2.

Using the above metric, we calculated the neutron (three sets), X-ray, and overall χ^2 for all simulations using the CHARMM force field. The resulting lipid areas ranging from 57.5 to 67.2 Å^2 are shown in Fig. 3. The neutron χ^2 exhibits a minimum at $A = 62.0$ Å^2 (open triangles), and the X-ray χ^2 has a minimum at $A = 63.0$ Å^2 (open squares) – although the difference between $A = 62.0$ and 63.0 Å^2 for the X-ray χ^2, is small. An example of the model-free comparison between simulation and experimental form factors is shown in Fig. 4. The similar trends of the neutron and X-ray χ^2, in addition to the similar lipid areas, where the smallest neutron and X-ray χ^2 occurs (Fig. 3, $A = 62.0$–63.0 Å^2), strongly support the validity of the simulated POPS bilayer.[40] It should also be pointed out that the smallest overall χ^2 occurs at 62.0 Å^2 (open circles), a lipid area which is very close to the one predicted by SDP model analysis (*i.e.*, 62.7 Å^2).

3.3 Lateral bilayer area compressibility

The area compressibility modulus K_A is an intrinsic mechanical property of lipid bilayers and can be obtained from MD simulations either through quantifying thermal fluctuation amplitudes or from the surface tension at several different lipid areas.[23] Using the method described in the Materials and

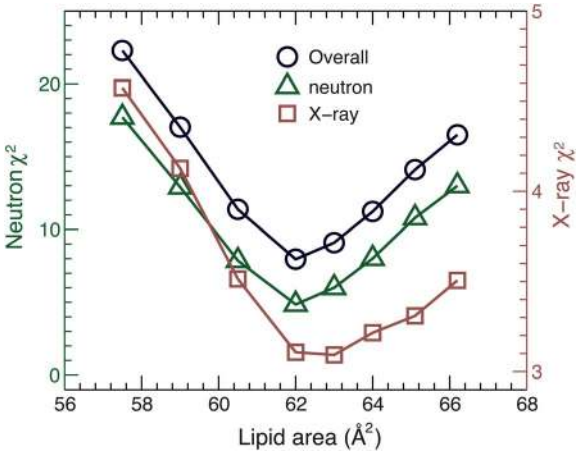

Fig. 3 Model-free comparison between experimental and simulated form factors using the CHARMM force field for different lipid areas. Three types of χ^2 were plotted. The neutron χ^2 (open triangle, left axis) was obtained by summing the squares of the neutron form factor differences at 3 D_2O concentrations, after being weighted by their experimental uncertainties and number of data points. The X-ray χ^2 (open square, right axis) was obtained in a similar fashion, except that there is only one X-ray data set. The overall χ^2 (open circle, left axis) is a combination of the neutron and X-ray χ^2.

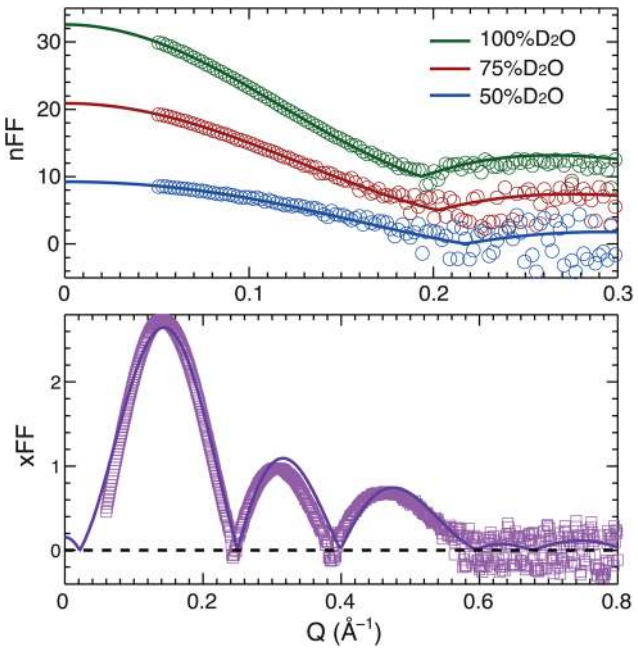

Fig. 4 Model-free comparison between experimental scattering data and a simulated POPS bilayer with $A = 62.0$ Å^2. The different contrast experimental neutron and X-ray form factors (symbols) are the same as those used in the SDP model analysis (Fig. 2). The corresponding simulation form factors (solid lines) were calculated from atom number density distributions using NAP_nT simulations. Each experimental form factor was scaled by a constant to minimize the reduced χ^2, after taking experimental uncertainties into account.

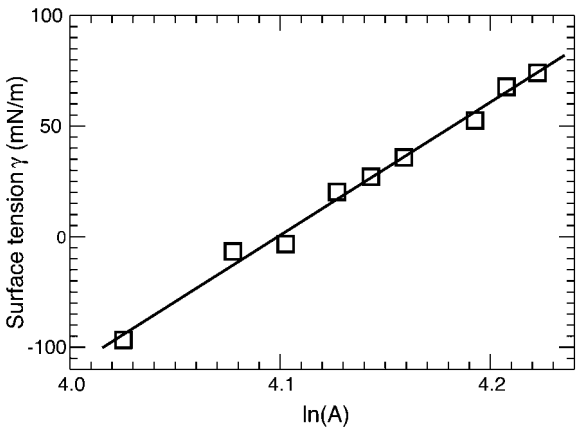

Fig. 5 Lateral surface tension applied to a POPS bilayer as a function of lipid area. The linear fit to the data (solid line) resulted in a bilayer area compressibility K_A of 601 mN m^{-1}.

Methods, we calculated the surface tension of POPS bilayers at different lipid areas (Fig. 5, CHARMM force field simulations). A linear fit resulted in a K_A of 601 mN m^{-1}. As discussed by Waheed and Edholm,[23] K_A is influenced both by sampling time and system size. For simulations on a time scale of 100 ns and a system size of 100 lipids per monolayer, K_A has an error of about 10%.[23] Our estimate of 601 ± 60 mN m^{-1} for the K_A of a POPS bilayer is about two times the value of 250–300 mN m^{-1} found for fluid-phase PC bilayers.[23,40–42]

3.4 Molecular features inferred from the "best" simulated bilayer

The model-free comparison presented in Section 3.2 lends support to area-constrained bilayer simulations that are capable of reproducing experimental SANS and SAXS signals. In this section we will describe some of the important findings regarding POPS bilayers, which were obtained from all-atom simulations using the CHARMM force field at $A = 62.0$ Å^2.

To understand the molecular interactions taking place between the charged PS headgroups and the surrounding counterions, we calculated volume averaged radial distribution functions (RDFs) for Na^+ ions with respect to different lipid oxygen atoms. These results are summarized in Fig. 6. Well-resolved peaks were identified between Na^+ ions and three types of oxygen atoms. Moreover, based on the magnitude (or integral) of the RDF peaks near 2.3 Å, it was found that Na^+ ions interact most strongly with the terminal carboxylic oxygen, followed by the phosphate oxygen and lastly, by the backbone carbonyl oxygen (weakest interaction). The decreasing affinity of Na^+ ions for lipid oxygens, which are located further from the aqueous phase into the lipid's backbone region, can be rationalized as follows. First, electrostatic interactions dominate the binding affinity of Na^+ such that the less polarized backbone carbonyl oxygen has a weaker affinity for Na^+ than the negatively charged carboxylic and phosphate oxygens. Second, due to the disposition of the serine and phosphate groups, the serine side chain is more exposed to the aqueous phase, thus enabling serine carboxylate to accommodate more neighboring Na^+ ions.

To visualize the Na^+ ion distribution near PS headgroups, a snapshot is shown in Fig. 7. It is clear that Na^+ ions are located in cages framed by neighboring water molecules and negatively charged lipid oxygens. The cage geometry changes in order to accommodate one or more Na^+ ions. When only one Na^+ is present within the cage, the total number of water and lipid oxygens is about 6–7. When two Na^+ are present in the cage, the average number of total water and lipid oxygens shielding each ion decreases, primarily due to the cooperative effect between the two Na^+ ions within the cage (*i.e.*, Na^+ ions partially shield

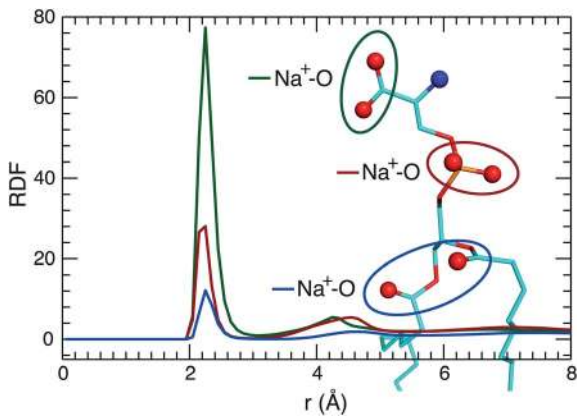

Fig. 6 RDFs of Na^+ ions with respect to POPS carboxylic (green), phosphate (firebrick), and backbone carbonyl (marine) oxygens.

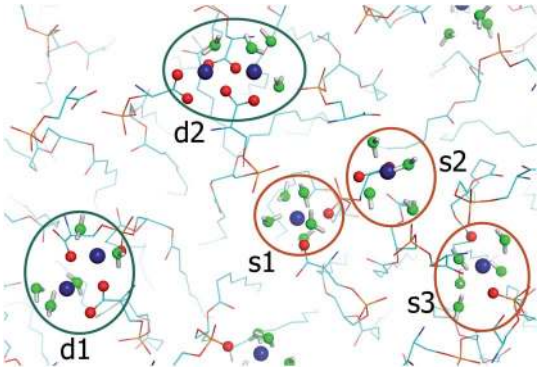

Fig. 7 Interactions of Na^+ ions with lipid and water molecules. A snapshot from NAP_nT simulations depicting the packing of water and lipid oxygens surrounding Na^+ ions. The nearby lipid carboxylic and phosphate oxygens (within 3 Å of Na^+ ions) are shown as red spheres, the nearby water oxygens (within 3 Å of Na^+ ions) are depicted as green spheres, and the Na^+ ions are shown as deep blue spheres. The remainder parts of lipids are depicted as thin sticks. Ellipses highlight two types of Na^+ cages (*i.e.*, s1, s2 and s3 correspond to single-Na^+ cage, and d1 and d2 correspond to double-Na^+ cage).

each other). PS lipids, therefore, seem to reduce the number of water molecules associated with interfacial Na^+ ions.[43]

In addition to lipid–ion interactions, we also explored the role of lipid–lipid interactions in stabilizing PS bilayer organization. RDFs between the positively charged ammonium nitrogen of the terminal serine and different oxygen atoms show that H-bonding and electrostatic interactions play a central role, as indicated by the prominent peaks near 2.7 Å between the ammonium nitrogen and carboxylic oxygen, and between the ammonium nitrogen and phosphate oxygen (Fig. 8). A significantly smaller peak, at a similar distance, was also identified between the ammonium nitrogen and backbone carbonyl oxygen, suggesting the presence of weak H-bonds. We note that the RDFs were calculated by counting only inter-lipid atom pairs (*i.e.*, atom pairs belonging to the same lipid were excluded). This method avoids counting intra-lipid pairs, thus eliminating effects arising from the close proximity between the ammonium nitrogen and carboxylic oxygen within the serine moiety. It is noteworthy that the diminished affinity of the backbone carbonyl oxygen to the ammonium nitrogen of POPS observed here is different than that reported in a previous study, where similar affinities of DPPS' ammonium to its carboxylic, phosphate, and backbone carbonyl oxygens were observed.[44] Two examples of inter-lipid interactions are illustrated in Fig. 9, depicting ammonium–carboxylate interactions (Fig. 9A) and ammonium–phosphate interactions (Fig. 9B).

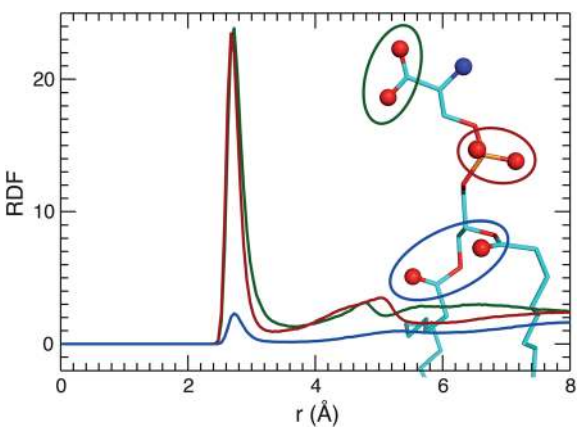

Fig. 8 Self-avoided inter-lipid interactions. RDFs were calculated between the ammonium nitrogen and three types of oxygens, namely carboxylic (green), phosphate (firebrick), and backbone carbonyl (marine) oxygens. To eliminate close proximity effects between the ammonium and the carboxylate moieties within a given lipid molecule, only inter-lipid pairs were calculated.

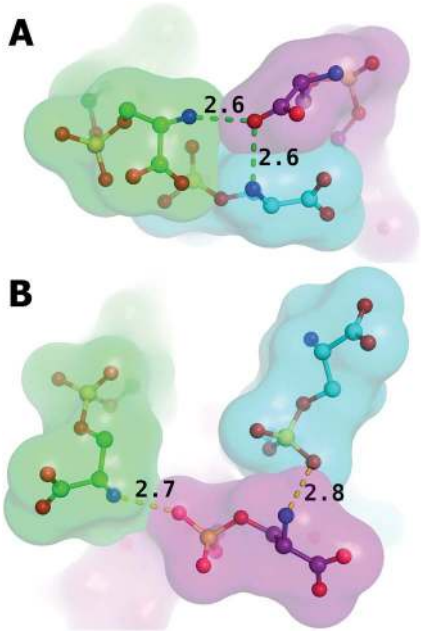

Fig. 9 Lipid–lipid interactions in the headgroup region. (A) Interactions between neighboring lipid ammonium and carboxylic oxygens (highlighted by green dashed lines). The oxygen–nitrogen distances are shown in units of Å. Three lipids are shown in ball-stick representation with semi-transparent surfaces. The oxygen, nitrogen and phosphorus atoms are colored in red, blue and orange, respectively. (B) Interactions between neighboring lipid ammonium and phosphate oxygens (highlighted by yellow dashed lines).

4. Discussion

4.1 Structural properties of the PS lipid bilayer

Because commonly used neutron and X-ray wavelengths are on the order of angstroms, SANS and SAXS are suitable probes for elucidating the structure of fluid lipid bilayers. By jointly refining SANS and SAXS data against a unified SDP model, we obtained a POPS lipid area of 62.7 $Å^2$ at 25 °C. The model used three Gaussian functions to describe the PS headgoup. We also used a model with two Gaussian functions for the headgroup (*i.e.*, one Gaussian function for the carbonyl-glycerol backbone and another for the phosphate and serine), which yielded a lipid area of 62.5 $Å^2$ (Fig. S4 in the ESI†), suggesting that the SDP analysis is insensitive to different atomic groupings within the PS headgroup.

To assess the effect of temperature on PS structure, we also studied POPS bilayers at 35, 45 and 55 °C using the same SDP model analysis. The resultant lipid areas as a function of temperature are shown in Fig. 10, along with data for the zwitterionic POPC lipid. It is clear that at a given temperature, POPS and POPC have similar lipid areas, implying that the negative charge associated with POPS does not have a large impact on lipid bilayer packing. This is consistent with an earlier study of 1,2-dioleoyl-*sn*-glycero-3-phosphatidylserine (DOPS) using X-ray diffraction data alone.[45] The authors reported a lipid area of 65.3 Å^2 for DOPS at 30 °C, a value similar to a lipid area of 67.4 Å^2 reported for its zwitterionic counterpart 1,2-dioleoyl-*sn*-glycero-3-phosphatidylcholine (DOPC).[38]

More recently, Venable *et al.* studied the effect of Na^+ ion Lennard–Jones radii on POPS bilayer structure.[10] They found that the simulated bilayer with an area per lipid of 58.4 Å^2 agreed best with their nuclear magnetic resonance (NMR) deuterium order parameters. However, when compared to their NMR data, it is clear that their best simulated bilayer exhibits greater chain order (*i.e.*, smaller lipid area). Their NMR data thus appears to be consistent with our result, where POPS has a lipid area larger than 58.4 Å^2 (*i.e.*, 62.7 Å^2).

It is important to validate MD simulations of PS lipid bilayers[9,10,44,46–48] using experimental data. Here we employed an approach devised by Braun *et al.*,[40] where multiple sets of MD simulations were performed with different (constrained) lipid areas. By comparing χ^2 between simulated and experimental form factors (eqn (3)), an optimal simulated bilayer was identified. A second criterion comes from the consideration that the χ^2 minimum for neutron and X-ray form factors should occur at the same (or at least similar) lipid area.[40] This is confirmed by data in Fig. 3, which shows the trend of individual neutron and X-ray χ^2. A distinct advantage of our approach is that it can be used for the structural determination of lipid bilayers doped with other molecules. For example, it is not uncommon to encounter situations where a peptide's conformation in a lipid bilayer is not known. In such a case, by performing a series of simulations with different peptide conformations, the correct peptide/lipid bilayer structure can be obtained when the simulated system is found to agree with the experimental scattering data.[49]

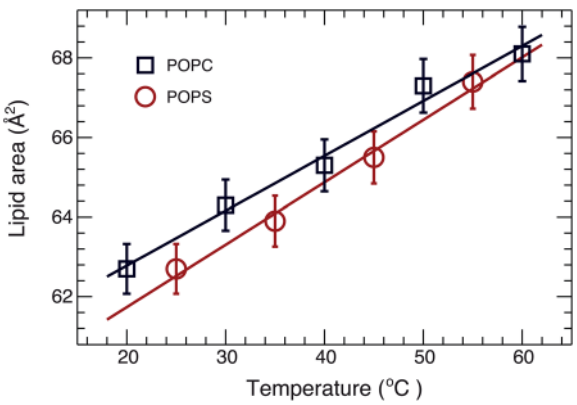

Fig. 10 Effect of the headgroup moiety on lipid bilayer structure. POPS lipid areas as a function of temperature are from this study (green circles). The lipid areas for POPC (black squares) are from Kučerka *et al.*[11]

4.2 Mechanical properties of POPS bilayer

Lipid membranes are dynamic and flexible entities, a prerequisite for many biological processes. In addition to their static structural properties, their mechanical properties are also important. For example, membrane bending rigidity plays an essential role in cell endocytosis and exocytosis, cell division, and viral fusion. Similarly, membrane area compressibility characterizes how easily a membrane can be laterally stretched or compressed, a feature most likely important in mediating membrane protein functions, such as ion channel conductance.[50]

By quantifying the relationship between surface tension and lipid area, the lipid bilayer area compressibility modulus K_A can be determined. From our simulations of POPS bilayers using the CHARMM force field, K_A was found to be 601 ± 60 mN m^{-1}, a value considerably larger than that for PC bilayers, which was experimentally determined to be about 250 mN m^{-1},[41,42] and about 300 mN m^{-1} from simulations.[23,40] The larger K_A for a POPS bilayer is consistent with an earlier study of DOPS multilamellar vesicles,[45] where it was found that for a given water content, DOPS bilayers exhibit smaller thermal fluctuations than DOPC bilayers. Moreover, ^{31}P-chemical shift NMR measurements indicated that the DOPS headgroup was less susceptible to external perturbations induced by osmotic pressure. Based on these data, it was concluded that DOPS bilayers possess a larger bending rigidity than their PC counterparts.[45]

In contrast to pure PS bilayers, the addition of 16% POPS to 1-stearoyl-2-oleoyl-*sn*-glycero-3-phosphatidylcholine (SOPC) bilayers results in no significant change to the overall bilayer bending rigidity.[51] Similarly, a small fraction of DOPS induces negligible perturbation to 1,2-dioleoyl-*sn*-glycero-3-phosphatidylethanolamine's (DOPE) bending modulus in the H_{II} phase.[52] The observation that bilayers composed of PS lipids exhibit a large K_A, while bilayers composed of PS and neutral lipids exhibit a small K_A, can be rationalized as follows. In the case of PS bilayers, the cooperative lipid–lipid associations facilitated by long-range electrostatic interactions confer substantial resistance to lateral deformation (Fig. 9). However, the presence of neutral lipids disrupts the electrostatic network between PS lipids, thus making the mixed lipid bilayer more susceptible to lateral deformation. One implication of this is that membranes with PS-rich domains will exhibit a larger K_A than randomly mixed PS and neutral lipids.

4.3 Molecular interactions within a POPS bilayer inferred from MD simulations

The model-free comparison (Fig. 3 and 4) indicates that simulated bilayers with an average lipid area of 62.0 Å^2 represent the most physically realistic POPS bilayer. Using this criterion, we derived several important molecular features of the POPS bilayer, which was simulated at $A = 62.0$ Å^2 using the CHARMM force field. Specifically, we found that PS headgroups form a

large network stabilized by long-range electrostatic interactions (Fig. 9). We also found that the headgroup's terminal serine plays a central role in lipid–lipid interactions. The unique capability of the serine group to promote inter-lipid interactions might be essential for enabling the participation of PS in various cellular functions. For example, externalization of PS lipids could give rise to the formation of PS-rich domains in the outer plasma membrane. Such domains, or serine facilitated lipid–lipid networks, could serve as hallmarks for apoptosis, which could be detected and targeted by extracellular partners, leading to downstream events associated with programmed cell death.

In addition to lipid–lipid interactions, a pairing between counterions and POPS headgroups was also observed. We found that the majority of Na^+ ions associate with the carboxylate and phosphate groups (Fig. 6). This result is in contrast to recent simulations of a binary mixture composed of POPC and POPS,[53] where it was reported that Na^+ ions penetrate deep into the lipid bilayer and preferentially associate with the backbone carbonyl oxygen. A similar result was reported for DPPS bilayers.[43] On the other hand, our result is consistent with the simulation work of Polyansky *et al.*, who reported a preferential association between Na^+ ions and the carboxylate and phosphate oxygens, but not the backbone carbonyl oxygen.[47] Presumably, counterions can be biased toward different lipid moieties depending on the details of the simulation force field. Validation protocols, such as comparing the scattering signal of simulated bilayers to experimental data, are therefore necessary for drawing reliable conclusions derived from MD simulation data.

5. Conclusion

In the present study we developed an SDP model for the POPS bilayer, which was aided by MD simulations. The model was then used to jointly refine different contrast SANS and SAXS data, yielding a lipid area of 62.7 $Å^2$ at 25 °C. Multiple sets of simulations were then performed with the lipid area constrained at discrete values. This resulted in an optimal simulated POPS bilayer (minimal overall χ^2) from which detailed molecular features were determined. Specifically, we found that Na^+ ions are coordinated in cages and preferentially interact with the lipid's carboxylate and phosphate groups. In addition, we found that neighboring PS lipids interact strongly with each other, an interaction facilitated by the positively charged ammonium and the negatively charged carboxylate and phosphate within the headgroup. Long-range inter-lipid electrostatic interactions, which are absent in neutral lipids, promote PS lipid cross-talk, and may be an important feature of PS participation in various cell phenomena, including programmed cell death. The headgroup network formed by PS lipids also suggests that the PS headgroup should not be treated as a point charge, but rather a polarized moiety with positive and negative charges dispersed among its different groups. Such a picture may be important when considering PS-specific targeting by anionic proteins and peptides.[6] Finally, by quantifying surface tension and lipid area deformation, we found that POPS bilayers exhibit a much larger area compressibility than bilayers composed of neutral lipids. This could have important implications for processes in which membrane material properties play a significant role, including the regulation of membrane ion channel permeability.[50]

Acknowledgements

We thank John Nagle and Drew Marquardt for discussions. Simulations using the GROMACS force field were performed partly using HPC resources from GENCI-CINES (Grant 2012–076353). Simulations using the CHARMM force field used the resources of the National Energy Research Scientific Computing Center, which is supported by the Office of Science of the U.S. Department of Energy under Contract no. DE-AC02-05CH11231. Support was received from the Laboratory Directed Research and Development Program (J.K.) of Oak Ridge National Laboratory (ORNL), managed by UT-Battelle, LLC, for the U.S. Department of Energy (DOE) under contract no. DE-AC05-00OR2275. This work acknowledges additional support from the DOE Office of Biological and Environmental Research (BER), for use of the Bio-SANS instrument at the ORNL Center for Structural Molecular Biology (CSMB), and from the Scientific User Facilities Division of the DOE Office of Basic Energy Sciences (BES), for use of the EQ-SANS instrument at the ORNL Spallation Neutron Source. SAXS data were collected at the Cornell High Energy Synchrotron Source (CHESS), which is supported by the National Science Foundation and the National Institutes of Health/National Institute of General Medical Sciences under NSF award DMR-0936384. DPT is an Alberta Innovates Health Solutions Scientist and Alberta Innovate Technology Futures Strategic Chair in (Bio) Molecular Simulation. Work in DPT's group is supported by the Natural Sciences and Engineering Research Council (Canada).

References

1 P. A. Leventis and S. Grinstein, *Annu. Rev. Biophys.*, 2010, **39**, 407–427.
2 M. A. Lemmon, *Nat. Rev. Mol. Cell Biol.*, 2008, **9**, 99–111.
3 M. K. Callahan, P. M. Popernack, S. Tsutsui, L. Truong, R. A. Schlegel and A. J. Henderson, *J. Immunol.*, 2003, **170**, 4840–4845.
4 E. Farge, *Biophys. J.*, 1995, **69**, 2501–2506.
5 P. Williamson, E. M. Bevers, E. F. Smeets, P. Comfurius, R. A. Schlegel and R. F. A. Zwaal, *Biochemistry*, 1995, **34**, 10448–10455.
6 G. D. Fairn, M. Hermansson, P. Somerharju and S. Grinstein, *Nat. Cell Biol.*, 2011, **13**, 1424–1430.
7 A. G. Buckland and D. C. Wilton, *Biochim. Biophys. Acta, Mol. Cell Biol. Lipids*, 2000, **1483**, 199–216.
8 S. H. Lee, X. W. Meng, K. S. Flatten, D. A. Loegering and S. H. Kaufmann, *Cell Death Differ.*, 2013, **20**, 64–76.
9 P. Mukhopadhyay, L. Monticelli and D. P. Tieleman, *Biophys. J.*, 2004, **86**, 1601–1609.
10 R. M. Venable, Y. Luo, K. Gawrisch, B. Roux and R. W. Pastor, *J. Phys. Chem. B*, 2013, **117**, 10183–10192.

11 N. Kučerka, M. P. Nieh and J. Katsaras, *Biochim. Biophys. Acta, Biomembr.*, 2011, **1808**, 2761–2771.
12 F. A. Heberle, J. J. Pan, R. F. Standaert, P. Drazba, N. Kučerka and J. Katsaras, *Eur. Biophys. J. Biophys. Lett.*, 2012, **41**, 875–890.
13 S. Jo, J. B. Lim, J. B. Klauda and W. Im, *Biophys. J.*, 2009, **97**, 50–58.
14 J. C. Phillips, R. Braun, W. Wang, J. Gumbart, E. Tajkhorshid, E. Villa, C. Chipot, R. D. Skeel, L. Kale and K. Schulten, *J. Comput. Chem.*, 2005, **26**, 1781–1802.
15 J. B. Klauda, R. M. Venable, J. A. Freites, J. W. O'Connor, D. J. Tobias, C. Mondragon-Ramirez, I. Vorobyov, A. D. MacKerell and R. W. Pastor, *J. Phys. Chem. B*, 2010, **114**, 7830–7843.
16 S. E. Feller, D. X. Yin, R. W. Pastor and A. D. MacKerell, *Biophys. J.*, 1997, **73**, 2269–2279.
17 T. Darden, D. York and L. Pedersen, *J. Chem. Phys.*, 1993, **98**, 10089–10092.
18 U. Essmann, L. Perera, M. L. Berkowitz, T. Darden, H. Lee and L. G. Pedersen, *J. Chem. Phys.*, 1995, **103**, 8577–8593.
19 M. Tuckerman, B. J. Berne and G. J. Martyna, *J. Chem. Phys.*, 1992, **97**, 1990–2001.
20 J. P. Ryckaert, G. Ciccotti and H. J. C. Berendsen, *J. Comput. Phys.*, 1977, **23**, 327–341.
21 G. J. Martyna, D. J. Tobias and M. L. Klein, *J. Chem. Phys.*, 1994, **101**, 4177–4189.
22 S. E. Feller, Y. H. Zhang, R. W. Pastor and B. R. Brooks, *J. Chem. Phys.*, 1995, **103**, 4613–4621.
23 Q. Waheed and O. Edholm, *Biophys. J.*, 2009, **97**, 2754–2760.
24 E. Lindahl and O. Edholm, *J. Chem. Phys.*, 2000, **113**, 3882–3893.
25 J. Sonne, F. Y. Hansen and G. H. Peters, *J. Chem. Phys.*, 2005, **122**, 124903.
26 O. Berger, O. Edholm and F. Jahnig, *Biophys. J.*, 1997, **72**, 2002–2013.
27 W. L. Jorgensen, J. D. Madura and C. J. Swenson, *J. Am. Chem. Soc.*, 1984, **106**, 6638–6646.
28 W. L. Jorgensen, D. S. Maxwell and J. TiradoRives, *J. Am. Chem. Soc.*, 1996, **118**, 11225–11236.
29 S. W. Chiu, M. Clark, V. Balaji, S. Subramaniam, H. L. Scott and E. Jakobsson, *Biophys. J.*, 1995, **69**, 1230–1245.
30 W. F. van Gunsteren and H. J. C. Berendsen, *Gromos-87 manual*, Groningen, 1987.
31 B. Hess, C. Kutzner, D. van der Spoel and E. Lindahl, *J. Chem. Theory Comput.*, 2008, **4**, 435–447.
32 M. Parrinello and A. Rahman, *J. Appl. Phys.*, 1981, **52**, 7182–7190.
33 G. Bussi, D. Donadio and M. Parrinello, *J. Chem. Phys.*, 2007, **126**, 014101.
34 S. Miyamoto and P. A. Kollman, *J. Comput. Chem.*, 1992, **13**, 952–962.
35 B. Hess, H. Bekker, H. J. C. Berendsen and J. G. E. M. Fraaije, *J. Comput. Chem.*, 1997, **18**, 1463–1472.
36 R. Kausik and S. Han, *Phys. Chem. Chem. Phys.*, 2011, **13**, 7732–7746.
37 K. Gawrisch, H. C. Gaede, M. Mihailescu and S. H. White, *Eur. Biophys. J.*, 2007, **36**, 281–291.
38 N. Kučerka, J. F. Nagle, J. N. Sachs, S. E. Feller, J. Pencer, A. Jackson and J. Katsaras, *Biophys. J.*, 2008, **95**, 2356–2367.
39 N. Kučerka, B. W. Holland, C. G. Gray, B. Tomberli and J. Katsaras, *J. Phys. Chem. B*, 2012, **116**, 232–239.
40 A. R. Braun, J. N. Sachs and J. F. Nagle, *J. Phys. Chem. B*, 2013, **117**, 5065–5072.
41 W. Rawicz, K. C. Olbrich, T. McIntosh, D. Needham and E. Evans, *Biophys. J.*, 2000, **79**, 328–339.
42 J. Pan, S. Tristram-Nagle, N. Kučerka and J. F. Nagle, *Biophys. J.*, 2008, **94**, 117–124.
43 S. A. Pandit, D. Bostick and M. L. Berkowitz, *Biophys. J.*, 2003, **84**, 3743–3750.
44 S. A. Pandit and M. L. Berkowitz, *Biophys. J.*, 2002, **82**, 1818–1827.
45 H. I. Petrache, S. Tristram-Nagle, K. Gawrisch, D. Harries, V. A. Parsegian and J. F. Nagle, *Biophys. J.*, 2004, **86**, 1574–1586.
46 J. J. López Cascales, J. Garcia de laTorre, S. J. Marrink and H. J. C. Berendsen, *J. Chem. Phys.*, 1996, **104**, 2713–2720.
47 A. A. Polyansky, P. E. Volynsky, D. E. Nolde, A. S. Arseniev and R. G. Efremov, *J. Phys. Chem. B*, 2005, **109**, 15052–15059.
48 U. R. Pedersen, C. Leidy, P. Westh and G. H. Peters, *Biochim. Biophys. Acta, Biomembr.*, 2006, **1758**, 573–582.
49 J. J. Pan, D. P. Tieleman, J. F. Nagle, N. Kučerka and S. Tristram-Nagle, *Biochim. Biophys. Acta, Biomembr.*, 2009, **1788**, 1387–1397.
50 T. J. McIntosh and S. A. Simon, *Annu. Rev. Biophys. Biomol. Struct.*, 2006, **35**, 177–198.
51 J. Song and R. E. Waugh, *J. Biomech. Eng.*, 1990, **112**, 235–240.
52 N. Fuller, C. R. Benatti and R. P. Rand, *Biophys. J.*, 2003, **85**, 1667–1674.
53 P. Jurkiewicz, L. Cwiklik, A. Vojtiskova, P. Jungwirth and M. Hof, *Biochim. Biophys. Acta, Biomembr.*, 2012, **1818**, 609–616.

